

SatFusion: A Unified Framework for Enhancing Satellite IoT Images via Multi-Temporal and Multi-Source Data Fusion

Yufei Tong
Zhejiang University
Hangzhou, China
yufetong@zju.edu.cn

Yicheng Zhu
Zhejiang University of Technology
Hangzhou, China
zeeyc@zjut.edu.cn

Meng Xi
Zhejiang University
Hangzhou, China
ximeng@zju.edu.cn

Junfan Wang
32012 Lab, Huawei Technologies Co.,
Ltd.
Shenzhen, China
wangjunfan3@huawei.com

Guanjie Cheng[†]
Zhejiang University
Hangzhou, China
chengguanjie@zju.edu.cn

Kexu Lu
Shandong University
Jinan, China
lukexu@mail.sdu.edu.cn

Junqin Huang
Shanghai Jiao Tong University
Shanghai, China
junqin.huang@sjtu.edu.cn

Peihan Wu
Zhejiang University
Hangzhou, China
22321313@zju.edu.cn

Feiyi Chen
Zhejiang University
Hangzhou, China
chenfeiyi@zju.edu.cn

Xueqiang Yan
32012 Lab, Huawei Technologies Co.,
Ltd.
Shenzhen, China
yanxueqiang1@huawei.com

Shuiguang Deng
Zhejiang University
Hangzhou, China
dengsg@zju.edu.cn

Abstract

With the rapid advancement of the digital society, the proliferation of satellites in the Satellite Internet of Things (Sat-IoT) has led to the continuous accumulation of large-scale multi-temporal and multi-source images across diverse application scenarios. However, existing methods fail to fully exploit the complementary information embedded in both temporal and source dimensions. For example, Multi-Image Super-Resolution (MISR) enhances reconstruction quality by leveraging temporal complementarity across multiple observations, yet the limited fine-grained texture details in input images constrain its performance. Conversely, pansharpening integrates multi-source images by injecting high-frequency spatial information from panchromatic data, but typically relies on pre-interpolated low-resolution inputs and assumes noise-free alignment—making it highly sensitive to noise and misregistration. To address these issues, we propose **SatFusion: A Unified Framework for Enhancing Satellite IoT Images via Multi-Temporal and Multi-Source Data Fusion**. Specifically, *SatFusion*

first employs a Multi-Temporal Image Fusion (MTIF) module to achieve deep feature alignment with the panchromatic image. Then, a Multi-Source Image Fusion (MSIF) module injects fine-grained texture information from the panchromatic data. Finally, a Fusion Composition module adaptively integrates the complementary advantages of both modalities while dynamically refining spectral consistency, supervised by a weighted combination of multiple loss functions. Extensive experiments on the WorldStrat, WV3, QB, and GF2 datasets demonstrate that *SatFusion* significantly improves fusion quality, robustness under challenging conditions, and generalizability to real-world Sat-IoT scenarios. The code is available at: <https://github.com/dllgyufei/SatFusion.git>.

CCS Concepts

• Computing methodologies → Computer vision; • Computer systems organization → Sensor networks.

Keywords

Satellite IoT, Data Fusion, Multi-Image Super-Resolution, Pansharpening, Image reconstruction

ACM Reference Format:

Yufei Tong, Guanjie Cheng[†], Peihan Wu, Yicheng Zhu, Kexu Lu, Feiyi Chen, Meng Xi, Junqin Huang, Xueqiang Yan, Junfan Wang, and Shuiguang Deng. 2018. *SatFusion: A Unified Framework for Enhancing Satellite IoT Images via Multi-Temporal and Multi-Source Data Fusion*. In *Proceedings of Make sure to enter the correct conference title from your rights confirmation email (Conference acronym 'XX) ACM, New York, NY, USA, 13 pages. <https://doi.org/XXXXXXX.XXXXXXX>*

[†] Guanjie Cheng is the corresponding author.

Permission to make digital or hard copies of all or part of this work for personal or classroom use is granted without fee provided that copies are not made or distributed for profit or commercial advantage and that copies bear this notice and the full citation on the first page. Copyrights for components of this work owned by others than the author(s) must be honored. Abstracting with credit is permitted. To copy otherwise, or republish, to post on servers or to redistribute to lists, requires prior specific permission and/or a fee. Request permissions from permissions@acm.org.

Conference acronym 'XX, Woodstock, NY

© 2018 Copyright held by the owner/author(s). Publication rights licensed to ACM.

ACM ISBN 978-1-4503-XXXX-X/2018/06

<https://doi.org/XXXXXXX.XXXXXXX>

1 Introduction

With the rapid development of communication and computing technologies, the Satellite Internet of Things (Sat-IoT) and satellite computing are becoming key components of future communication and intelligent data processing infrastructures [21, 22, 27, 37]. By deploying globally distributed satellite constellations, Sat-IoT enables Earth observation and data transmission capabilities on a planetary scale. To further enhance the role of remote sensing imagery in various applications such as ground observation and smart cities [23, 37, 47], the demand for high-quality satellite images continues to grow. However, due to the constraints on satellite size and weight, the onboard imaging equipment often suffers from limited spatial resolution [6]. In addition, the inherent physical limitations of imaging sensors prevent them from simultaneously producing images with both high spatial resolution and high spectral resolution (i.e., with more spectral bands) [47], which restricts the further utilization of Sat-IoT imagery.

Low-Earth orbit (LEO) small satellites serve as the key foundation for constructing Sat-IoT systems, offering advantages such as short revisit cycles and low manufacturing costs [6]. These capabilities enable multiple satellites to frequently observe the same region, thereby acquiring a large volume of multi-temporal remote sensing images. Meanwhile, the use of different onboard imaging sensors across satellites leads to the generation of multi-source remote sensing images. As the number of observation satellites in Sat-IoT systems continues to grow, ground stations, as receiving terminals, must simultaneously process massive amounts of multi-temporal and multi-source imagery [13, 16, 24, 37, 38, 43]. The contradiction between the abundance of low-quality redundant data and the growing demand for high-quality imagery has become increasingly pronounced [25, 47], resulting in severe data backlog issues. Therefore, how to generate high-quality images from massive low-quality and redundant data has emerged as an urgent challenge to be addressed.

Multi-temporal data contain temporal complementary information [9], while multi-source images provide highly complementary spatial and spectral information [13]. Previous studies have conducted extensive research on multi-temporal data fusion (Multi-Image Super-Resolution, MISR) and multi-source data fusion (Pansharpening). However, existing approaches fail to simultaneously leverage the complementary information from both multi-temporal and multi-source images, leaving several key challenges unresolved: (1) Task separation and lack of a unified framework: The MISR and pansharpening networks are modeled independently [13, 24], making it difficult to jointly process multi-temporal and multi-source images in Sat-IoT scenarios. (2) Limited improvement in fusion and enhancement quality: In MISR, the input images usually contain limited fine-grained texture features, which constrains the quality of reconstructed outputs. (3) Significant gap between experimental settings and real satellite applications: Existing pansharpening methods typically construct synthetic datasets using the Wald protocol [36], where a single low-resolution multispectral image and a single high-resolution panchromatic image are spatially well-aligned and free from common noise in real-world conditions. Moreover, pansharpening relies on interpolating low-resolution images and spatially aligning them with panchromatic

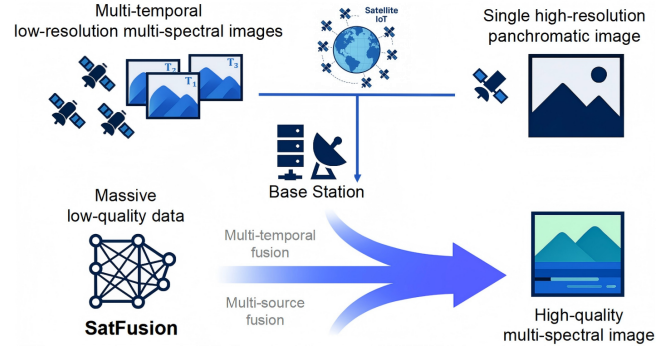


Figure 1: Overview of the *SatFusion* system. LEO satellites transmit low-quality images to ground stations, where *SatFusion* performs fusion-based reconstruction to enhance image quality and reduce redundancy.

images, which makes it highly sensitive to input quality and thus difficult to apply effectively in practice.

To address the aforementioned background and challenges, we propose *SatFusion*, a novel unified framework that collaboratively utilizes multi-temporal and multi-source images to reconstruct high-quality imagery. The framework employs a Multi-Temporal Image Fusion (MTIF) module to generate high-spatial-resolution deep features containing temporal complementary information, thereby achieving spatial alignment with the panchromatic image. By leveraging multi-temporal data, this module alleviates the limitations of pansharpening methods that rely on interpolation-based spatial alignment, which are often sensitive to input variations and difficult to apply in real-world conditions, thus enhancing robustness. The Multi-Source Image Fusion (MSIF) module injects fine-grained texture features from the panchromatic image to address the constrained output quality of MISR networks. Furthermore, a Fusion Composition Module adaptively integrates the complementary advantages of multi-temporal and multi-source images while adjusting spectral features, with reconstruction supervised by a weighted combination of multiple loss functions. The main technical contributions of this work are as follows:

(1) We propose a novel unified framework, *SatFusion*, which collaboratively utilizes multi-temporal and multi-source images to reconstruct high-quality imagery. To the best of our knowledge, this is the first work in the remote sensing domain that jointly optimizes multi-temporal and multi-source image fusion within a unified framework.

(2) As illustrated in Figure 1, *SatFusion* effectively bridges the gap between massive low-quality redundant data and the growing demand for high-quality imagery, providing an efficient and practical solution for Sat-IoT scenarios that require high-quality imaging.

(3) Extensive experiments on datasets including WorldStrat, WV3, QB, and GF2 demonstrate the superior reconstruction quality and robustness of *SatFusion* compared with existing methods.

2 Background

2.1 Multi-Temporal Data Fusion

Multi-temporal data fusion aims to integrate complementary information from multiple images of the same region captured at different times by the same sensor, thereby reconstructing a higher-quality image. A representative approach is Multi-Image Super-Resolution (MISR). As shown in Figure 2(a), the reconstruction process is formulated as:

$$SR = f_{\text{MISR}}(lr_1, lr_2, \dots, lr_T), \quad (1)$$

where the input set $\{lr_t\}_{t=1}^T \in \mathbb{R}^{\frac{H}{\gamma} \times \frac{W}{\gamma} \times C}$ consists of T low-resolution (LR) images, and the output $SR \in \mathbb{R}^{H \times W \times C}$ denotes a single high-resolution (HR) image. Here, H and W are spatial dimensions, γ is the upsampling factor, and C is the number of spectral channels.

In recent years, deep neural network-based methods have demonstrated outstanding performance in terms of accuracy and representational capacity. These include feature alignment based on convolutional neural networks (CNNs) [9, 32–34, 48], detail enhancement using generative adversarial networks (GANs) [40], and cross-temporal modeling with Transformers [2, 11, 26, 35, 41]. Nevertheless, since all LR inputs originate from the same modality, they lack sufficient high-frequency texture cues, which fundamentally limits the reconstruction fidelity.

2.2 Multi-Source Data Fusion

Multi-source data fusion aims to integrate complementary information from images of the same region captured by heterogeneous sensors, thereby reconstructing a higher-quality image. A representative task in this field is pansharpening (Sharpen). As shown in Figure 2(b), the fusion process can be formulated as:

$$SR = f_{\text{Sharpen}}(lrms, Pan), \quad (2)$$

where $lrms \in \mathbb{R}^{\frac{H}{\gamma} \times \frac{W}{\gamma} \times (C_{ms} > 1)}$ denotes a low-resolution multispectral (LRMS) image, and $Pan \in \mathbb{R}^{H \times W \times (C_{pan} = 1)}$ denotes a high-resolution panchromatic (HRPAN) image. The output $SR \in \mathbb{R}^{H \times W \times C_{ms}}$ is a high-resolution multispectral (HRMS) image with the same spectral channels as the MS input but upsampled by a factor of γ in spatial resolution. The introduction of CNNs [4, 12, 20, 49], GANs [51], Transformers [3, 31, 50], diffusion models [30, 42], and more recently Mamba architectures [15] has significantly improved the fusion accuracy and fidelity of pansharpening networks.

Despite these advances, existing pansharpening networks still face key limitations in real-world Sat-IoT settings. First, most methods rely on a single LRMS and single HRPAN input pair, lacking the ability to exploit abundant multi-temporal observations. Second, since the pioneering PNN model [28], nearly all subsequent works have followed the Wald protocol for dataset synthesis, which assumes perfect spatial alignment and noise-free conditions [36]. This setting diverges from practical Sat-IoT scenarios, where misalignment, blur, and sensor noise are common. Finally, as shown in Figure 2(b), most pansharpening networks first interpolate the input $lrms$ image to match the spatial dimensions of the Pan image before passing them to the fusion module. The fused features are then processed through either residual connections (Figure 2(d)) or direct outputs (Figure 2(c)) to produce SR . Such dependence on a single interpolated input makes these models highly sensitive to

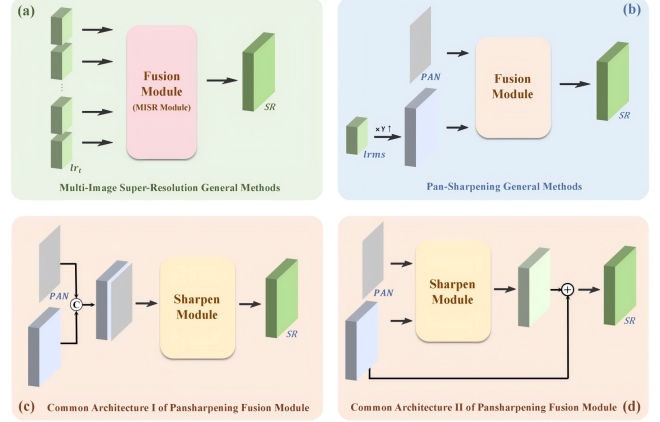


Figure 2: Overview of MISR and PanSharpening network general methods. (a) General methods of MISR networks; (b) General methods of PanSharpening networks; (c) Common architecture I of PanSharpening fusion module; (d) Common architecture II of PanSharpening fusion module.

LRMS image quality, further limiting robustness under real-world acquisition variability.

2.3 Data Processing Methods in Sat-IoT

In the Sat-IoT domain, **data selection** and **data fusion** are two primary strategies for managing the massive volume of remote sensing data. Data selection aims to identify high-quality samples, mitigating the conflict between redundant low-quality data and the demand for high-quality imagery. Early methods relied on manually defined rules, such as clarity or cloud coverage thresholds [52]. More recent studies leverage deep learning-based image quality assessment models [17–19, 29], where CNNs automatically learn discriminative features correlated with visual quality, achieving more accurate filtering. However, these approaches are limited to redundancy elimination and cannot synthesize new high-quality data, which constrains their contribution to overall data enhancement.

As discussed in Sections 2.1 and 2.2, data fusion aims to generate higher-quality images from existing datasets. With the rapid growth of Sat-IoT and the accumulation of both multi-temporal and multi-source imagery, exploiting the complementary relationships among heterogeneous datasets has become increasingly promising for real-world applications. To the best of our knowledge, only one concurrent work, [53], attempts to jointly utilize multi-temporal and multi-source imagery. However, their approach differs fundamentally from ours in both architectural design and motivation. Specifically, Ziaja *et al.* (2025) trained separate MISR and pansharpening networks and concatenated their outputs sequentially, without addressing the architectural limitations inherent to either model. This two-stage design lacks mutual feature interaction and fails to achieve unified optimization. In addition, their method focuses primarily on compounded resolution enhancement—where the MISR output ($\uparrow \times \alpha$) and HRPAN image serve as inputs to a pansharpening model that still relies on interpolation of low-resolution images for spatial alignment and generates a single super-resolved output

$(\uparrow \times \beta)$, yielding an overall gain of $(\uparrow \times \alpha \cdot \beta)$ —rather than addressing the robustness, noise sensitivity, and scalability challenges characteristic of practical Sat-IoT environments.

3 Problem Statement

3.1 Multi-Temporal and Multi-Source Image Fusion Framework

Previous studies cannot simultaneously exploit both multi-temporal and multi-source images in Sat-IoT. We propose a new problem that better fits real-world needs: how to leverage multi-temporal data (a set of LRMS images of the same location captured at different times or by different MS sensors) together with multi-source data (a single HRPAN image and LRMS images of the same location captured by different sensors) to generate a single HRMS image of high quality. The image reconstruction task is formally defined as:

$$SR = f_{\text{Reconstruct}}(lrms_1, lrms_2, \dots, lrms_T, Pan), \quad (3)$$

where the inputs $\{lrms_t\}_{t=1}^T \in \mathbb{R}^{\frac{H}{Y} \times \frac{W}{Y} \times C_{ms}}$ denote LRMS images, and $Pan \in \mathbb{R}^{H \times W \times C_{pan}}$ denotes one HRPAN image. The output is $SR \in \mathbb{R}^{H \times W \times C_{ms}}$, representing a HRMS image. The output image preserves the same number of spectral channels as the MS inputs, while being upsampled by a factor of γ in both spatial dimensions.

3.2 Design Challenges

Based on the problem formulation above, we identify two major challenges in designing a fusion framework. The first challenge lies in the fact that existing frameworks cannot jointly optimize multi-temporal and multi-source data. As discussed in Section 2, current frameworks each have their own limitations. Constructing a unified framework that organically integrates the optimization of multi-temporal data and multi-source data is nontrivial. Simply training existing multi-temporal and multi-source fusion networks separately and concatenating their outputs in sequence [53], or entirely discarding prior work, is insufficient.

The second challenge is the need for greater robustness. In real Sat-IoT systems, images often suffer from blur, noise, and imperfect alignment across acquisitions. Most existing studies assume clean and well-aligned inputs, focusing on architectural improvements to optimize performance metrics, which limits their applicability in practice. Our goal is to design a model that can maintain stable performance even under complex and imperfect conditions.

4 Methodology

4.1 Overall Architecture of *SatFusion*

SatFusion is designed to achieve the following objectives: (1) Construct a unified framework to jointly process multi-temporal and multi-source imagery; (2) Exploit the complementary information of multi-temporal and multi-source images to enhance the quality of the fused output; (3) Maintain robustness under complex real-world conditions; (4) Ensure scalability, such that the framework can be adapted to and extended from prior studies.

SatFusion takes as input a set of LRMS images $\{lrms_t\}_{t=1}^T \in \mathbb{R}^{\frac{H}{Y} \times \frac{W}{Y} \times C_{ms}}$ and a single HRPAN image $Pan \in \mathbb{R}^{H \times W \times (C_{pan}=1)}$. The output is a HRMS fused image $SR \in \mathbb{R}^{H \times W \times C_{ms}}$ that preserves both high spatial and spectral resolution.

The *SatFusion* framework consists of three key submodules: a multi-temporal image fusion module, a multi-source image fusion module, and a fusion composition module. The complete network structure is illustrated in Figure 3.

4.2 Implementation Details of Core Modules

Multi-temporal Image Fusion Module (MTIF). Its goal is to extract complementary information from multiple LRMS images $\{lrms_t\}_{t=1}^T \in \mathbb{R}^{\frac{H}{Y} \times \frac{W}{Y} \times C_{ms}}$ of the same region acquired by the same type of sensor, so as to generate a single super-resolved MS feature map $SR_{MTIF} \in \mathbb{R}^{H \times W \times C_{ms}}$, which is formally written as:

$$SR_{MTIF} = MTIF(lrms_1, lrms_2, \dots, lrms_T), \quad (4)$$

The MTIF module consists of an encoder, a multi-temporal image super-resolution(MISR) module, and a decoder. $\{lrms_t\}_{t=1}^T$ are passed through the encoder with shared parameters to extract their respective features $\{x_t^{\text{encode}}\}_{t=1}^T$:

$$x_t^{\text{encode}} = Encoder(lrms_t), \quad (5)$$

where the output features $\{x_t^{\text{encode}}\}_{t=1}^T \in \mathbb{R}^{\frac{H}{Y} \times \frac{W}{Y} \times C_{\text{hidden_encode}}}$, $Encoder$ denotes the convolutional encoder with shared parameters, and T represents the number of multi-temporal images. Then, $\{x_t^{\text{encode}}\}_{t=1}^T$ are processed by the MISR module to output the deep features of multi-temporal image fusion:

$$x^{\text{MISR}} = f_{\text{MISR}}(x_1^{\text{encode}}, x_2^{\text{encode}}, \dots, x_T^{\text{encode}}), \quad (6)$$

where the output fused features $x^{\text{MISR}} \in \mathbb{R}^{H \times W \times C_{\text{MISR}}}$, and f_{MISR} denotes the fusion module of the MISR network designed by previous researchers (MISR module, as shown in Figure 2(a)). Then x^{MISR} is processed by the decoder, and the output is the super-resolved deep feature SR_{MTIF} :

$$SR_{MTIF} = Decoder(x^{\text{MISR}}), \quad (7)$$

where the output super-resolved feature $SR_{MTIF} \in \mathbb{R}^{H \times W \times C_{ms}}$. The function of the decoder is to adjust the spatial feature dimensions of the image so that it aligns with the input HRPAN image Pan ; and to adjust the channel feature dimension of the image so that it matches the target image. We implement the decoder using a sub-pixel convolution (PixelShuffle) block:

$$x^{\text{PixelShuffleBlock}} = PixelShuffleBlock(Conv2d(x^{\text{MISR}})), \quad (8)$$

where $x^{\text{PixelShuffleBlock}} \in \mathbb{R}^{H' \times W' \times C_{ms}}$ is the feature map output by the PixelShuffle Block, and $Conv2d$ adjusts the channel dimension to be divisible by γ^2 , ensuring the correct operation of the sub-pixel convolution module. The sub-pixel convolution increases the spatial resolution of the feature maps by rearranging pixels from the channel dimension into the spatial dimension. When data enter the PixelShuffle Block, pixel rearrangement is performed first, followed by a stack of Conv, Batch Normalization, and PReLU functions to obtain the output. $x^{\text{PixelShuffleBlock}}$ is optionally processed by the *Resize* module:

$$SR_{MTIF} = \begin{cases} x^{\text{PixelShuffleBlock}}, & \text{if } H = H' \text{ and } W = W' \\ \text{Resize}(x^{\text{PixelShuffleBlock}}), & \text{otherwise} \end{cases} \quad (9)$$

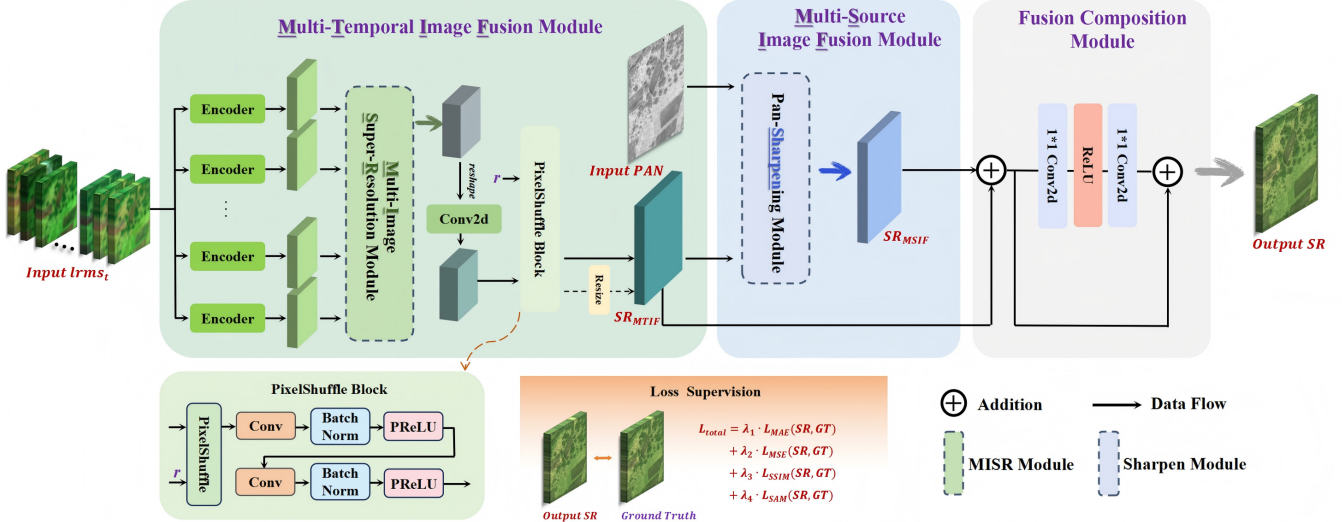


Figure 3: Architecture of *SatFusion*. The framework takes multiple multi-temporal LRMS images and a single HRPAN image as inputs. These are processed sequentially through the multi-temporal image fusion module, the multi-source image fusion module, and the fusion composition module, producing the final HRMS image.

where *Resize* adjusts the spatial dimensions by interpolation to ensure that the output features of the MTIF module are spatially aligned with the input *Pan*.

Multi-Source Image Fusion Module (MSIF). Its goal is to extract complementary information from multi-source images of the same region acquired by different sensors, thereby simultaneously preserving spatial details and spectral information. The inputs are the output SR_{MTIF} from the MTIF module and a single HRPAN image $Pan \in \mathbb{R}^{H \times W \times (C_{pan}=1)}$. The output is another super-resolved MS feature map SR_{MSIF} , formulated as:

$$SR_{MSIF} = MSIF(SR_{MTIF}, Pan), \quad (10)$$

The MSIF module is composed of a pansharpening module. By feeding SR_{MTIF} and Pan into the pansharpening module, the fused features SR_{MSIF} are obtained:

$$SR_{MSIF} = f_{Sharpen}(SR_{MTIF}, Pan), \quad (11)$$

Here, the fused features $SR_{MSIF} \in \mathbb{R}^{H \times W \times C_{ms}}$, and $f_{Sharpen}$ represents the fusion module of the pansharpening network designed by previous researchers (Sharpen module, as shown in Figure 2(c)(d)). The key difference from prior work lies in the fact that we take the multi-temporal fused features SR_{MSIF} together with Pan as inputs to the sharpen module, where the spatial dimensions of SR_{MSIF} and Pan are already aligned, rather than merely upsampling a single $lrms$ band by interpolation to match the resolution of Pan .

Fusion Composition Module. Its goal is to fuse the outputs of the MTIF module and the MSIF module, so as to adaptively exploit the advantages of both multi-temporal and multi-source image fusion. The inputs are the output SR_{MTIF} from the MTIF module and the output SR_{MSIF} from the MSIF module, and the output is the final single HRMS image SR . The Fusion composition module consists of residual connections and convolution adjustment operations, and

finally outputs SR :

$$SR = Conv(ReLU(Conv(SR_{MTIF} + SR_{MSIF}))). \quad (12)$$

Here, the output is the HRMS image $SR \in \mathbb{R}^{H \times W \times C_{ms}}$, and $Conv$ denotes a 2D convolution with kernel size 1×1 . The 1×1 convolution plays a role in adjusting spectral characteristics [32]. By placing the convolution operation after the residual connection, the model is encouraged to learn spectral features more effectively.

4.3 Loss Function

We adopt a supervised learning approach to train *SatFusion* in an end-to-end manner. We design a weighted combination of different loss functions to supervise the reconstruction results, jointly optimizing both texture features and spectral features of the images:

$$\begin{aligned} \mathcal{L}_{\text{total}} = & \lambda_1 \cdot \mathcal{L}_{\text{MAE}}(SR, GT) + \lambda_2 \cdot \mathcal{L}_{\text{MSE}}(SR, GT) \\ & + \lambda_3 \cdot \mathcal{L}_{\text{SSIM}}(SR, GT) + \lambda_4 \cdot \mathcal{L}_{\text{SAM}}(SR, GT) \end{aligned} \quad (13)$$

where $\lambda_1, \lambda_2, \lambda_3$, and λ_4 are the corresponding weights, satisfying $\lambda_1 + \lambda_2 + \lambda_3 + \lambda_4 = 1$. SR denotes the image output by *SatFusion*, and GT denotes the ground truth image. \mathcal{L}_{MAE} is the l_1 loss, and \mathcal{L}_{MSE} is the l_2 loss, both of which are commonly used to supervise the outputs of MISR and pansharpening networks. Prior works retained the same loss functions while modifying model architectures to ensure fair comparison. On top of these loss functions, we introduce new supervisory signals: $\mathcal{L}_{\text{SSIM}}$ is a texture loss function focusing on the learning of spatial features, while \mathcal{L}_{SAM} is a spectral loss function emphasizing the learning of spectral features.

Since discrepancies exist between the acquisition conditions of input images and the ground truth, SR and GT may exhibit horizontal/vertical shifts as well as overall brightness deviations. Following prior work, we perform brightness adjustment and boundary cropping before computing the loss in some experiments [2, 9, 33]. For

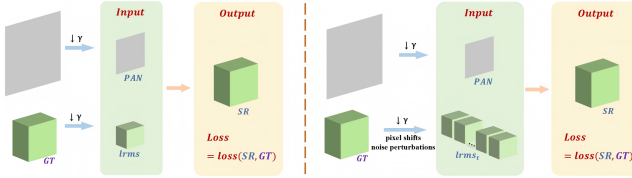


Figure 4: (left) Workflow of the conventional Wald protocol for dataset construction; (right) Workflow of the Wald protocol with introduced noise for dataset construction.

more details on *SatFusion*'s loss calculation, please refer to Appendix D. It is worth emphasizing that we ensure consistency in loss calculation during experiments. Specifically, when comparing *SatFusion* with baseline methods, we apply the same adjustment operations to SR before computing the loss, and use the same functions for loss computation across the entire training, validation, and testing pipeline. This guarantees that improvements in evaluation metrics directly demonstrate the effectiveness of the architecture.

5 Experiments

We conduct extensive experiments to address the questions:

RQ1: How does *SatFusion* perform compared with baseline models on datasets collected from real-world scenarios?

RQ2: How does *SatFusion* perform compared with baseline models on synthetic datasets constructed following the Wald protocol?

RQ3: How do the number of input multi-temporal images and the super-resolution scaling factor influence the performance of *SatFusion*?

RQ4: How do the loss function and the Fusion Module affect the performance of *SatFusion*?

RQ5: How does *SatFusion* perform compared with baseline models under challenging conditions such as image blurriness and large cross-modal discrepancies?

We answer **RQ1** and **RQ2** in the main experiments (Section 5.2), **RQ3** in the hyperparameter experiments (Appendix A), **RQ4** in the ablation studies (Appendix B), and **RQ5** in the robustness experiments (Appendix C).

5.1 Experimental Setup

Dataset. We conduct experiments on the WorldStrat [5], WV3, QB, and GF2 datasets [8]. WorldStrat data comes from real satellites without removing low-quality images, thus better reflecting real-world scenarios. Each location in this dataset consists of multiple multi-temporal LRMS images, one HRPAN image, and one HRMS image, which are commonly used for MISR network training. For the WV3, QB, and GF2 datasets, each location includes one HRPAN image and one LRMS image. Previous works commonly employed these datasets to construct synthetic datasets via the Wald protocol [36] for pansharpening network training.

We conduct experiments on both the real dataset and synthetic datasets constructed using the Wald protocol. It is worth noting that *SatFusion* takes multiple multi-temporal LRMS images and a single HRPAN image as input. However, as shown in Figure 4(left), prior pansharpening works use Wald protocol to construct synthetic *lrms* and *Pan* images as input, which has inherent idealized

limitations (Section 2.2). As shown in Figure 4(right), we introduce pixel shifts and noise perturbations into the Wald protocol to construct synthetic multi-temporal images $\{lrms_t\}_{t=1}^T$, which are then combined with the *Pan* image as the input of *SatFusion*. Experiments are conducted on both real datasets and synthetic datasets with added noise perturbations, making them more consistent with the data conditions in Sat-IoT scenarios.

Evaluation Methods and Metrics. We compare *SatFusion* against several MISR networks and pansharpening networks. We adopt PSNR, SSIM, SAM [46], and ERGAS [1] as quantitative evaluation metrics, and additionally provide reconstructed images and error maps for qualitative evaluation.

Implementation Details. We ensure consistency in the experimental setup, meaning that when comparing *SatFusion* with baseline methods, training parameters (e.g., epochs, batch size, optimizer, etc.) and data parameters (e.g., H , W , C_{ms} , γ , T , etc.) are kept the same. For more details on the experimental parameter settings, please refer to Appendix E.

5.2 Main Experiments

We conduct experiments on both real and synthetic datasets to answer **RQ1** and **RQ2**.

On the real dataset, we validate that the *SatFusion* framework is beneficial for enhancing both MISR and Pansharpening networks. We conduct experiments on the original WorldStrat dataset, where *SatFusion* takes $\{lrms_t\}_{t=1}^{T=8}$ and *Pan* as inputs, the MISR network takes $\{lrms_t\}_{t=1}^{T=8}$ as input, and the Pansharpening network takes a randomly selected single *lrms* and *Pan* as inputs.

As shown in Table 1(a), *SatFusion* achieves notable improvements over both MISR and Pansharpening networks in quantitative metrics. Specifically, compared with MISR, the average PSNR is improved by 27.1% and ERGAS by 73.6%; compared with Pansharpening, the average PSNR and ERGAS are improved by 2.6% and 13.9%, respectively. On the WorldStrat test set, *SatFusion* demonstrates a clear enhancement in the reconstructed image quality, indicating its capability to adaptively leverage the strengths of both MISR and Pansharpening methods. We visualize the fused results and their corresponding PSNR values in Figure 5.

On the synthetic dataset, we validate that the *SatFusion* framework is beneficial for enhancing Pansharpening networks. Using the WorldStrat, WV3, QB, and GF2 datasets, we construct synthetic multi-temporal images $\{lrms_t\}_{t=1}^T$ with pixel shifts and noise disturbances introduced through the Wald protocol. *SatFusion* takes $\{lrms_t\}_{t=1}^{T=8}$ and *Pan* as inputs, while the Pansharpening network takes a randomly selected *lrms* and *Pan* as inputs.

As shown in Table 2 and Table 1(b), *SatFusion* significantly improves the quality of the fused images on the test sets of the synthetic datasets. We visualize the fused images and the error maps between the *SR* and the *GT* in Figure 6, verifying its ability to adaptively fuse multi-source features in scenarios with complex disturbances. This further demonstrates the effectiveness and advantages of *SatFusion* in integrating MISR and Pansharpening networks.

Table 1: Metrics on the WorldStrat Real (a) and Synthetic (b) datasets.

Methods	(a) Metrics on the WorldStrat Real Dataset						(b) Metrics on the WorldStrat Synthetic Dataset						#Params	
	PSNR↑	SSIM↑	SAM↓	ERGAS↓	MAE↓	MSE↓	PSNR↑	SSIM↑	SAM↓	ERGAS↓	MAE↓	MSE↓		
MISR	SRCCNN [10]	36.9638	0.8761	2.4066	9.0150	1.4579	9.6667	38.0880	0.8721	2.4173	6.3953	1.1857	5.7754	1778.77K
	HighRes-Net [9]	37.1057	0.8795	2.2328	9.4426	1.4355	9.4041	38.2952	0.8774	2.1054	6.1646	1.1363	5.2376	1631.44K
	RAMS [33]	37.0479	0.8774	2.2741	8.9813	1.4415	9.3536	40.4698	0.9201	1.6896	4.6930	0.8822	3.0800	492.68K
	TR-MISR [2]	37.0769	0.8785	2.2514	9.2554	1.4204	9.1929	38.7603	0.8865	1.8453	5.8359	1.0752	4.7981	618.00K
Sharpen	PNN [28]	46.0607	0.9864	2.2886	2.7871	0.4489	0.5612	46.7428	0.9917	1.8818	2.2968	0.4098	0.4509	230.67K
	PanNet [44]	46.1507	0.9847	2.1982	2.7560	0.4444	0.5470	46.8736	0.9897	1.9171	2.2220	0.3946	0.4166	463.31K
	INNformer [50]	46.2420	0.9853	2.2742	2.7035	0.4374	0.5213	46.9651	0.9897	2.0786	2.2591	0.3964	0.4379	218.92K
	Pan-Mamba [15]	45.1075	0.9843	2.9452	3.0223	0.4864	0.5926	47.3198	0.9923	1.8901	2.1413	0.3817	0.3997	634.10K
MISR														
Sharpen														
SatFusion	SRCCNN	47.2319	0.9898	2.0082	2.3719	0.3876	0.4288	47.6045	0.9916	1.8327	2.0977	0.3648	0.3638	1853.20K
	PanNet	47.3235	0.9900	1.9322	2.3170	0.3843	0.4240	48.0213	0.9912	1.7359	2.0567	0.3505	0.3451	2085.84K
	INNformer	47.2222	0.9872	2.0510	2.3210	0.3834	0.4187	47.6046	0.9883	1.8385	2.1348	0.3641	0.3769	1841.45K
	Pan-Mamba	45.6298	0.9889	2.5037	2.8812	0.4738	0.5822	46.8506	0.9921	2.0728	2.3695	0.4016	0.4352	2256.63K
MISR	PNN	47.3835	0.9914	1.9368	2.3304	0.3817	0.4231	48.0743	0.9928	1.7433	2.0466	0.3472	0.3421	1705.87K
	PanNet	47.3911	0.9902	1.9508	2.3232	0.3819	0.4193	48.0657	0.9911	1.7094	2.0661	0.3443	0.3313	1938.51K
	INNformer	47.4021	0.9902	1.8958	2.3094	0.3834	0.4202	47.9931	0.9928	1.7546	2.0119	0.3488	0.3466	1694.12K
	Pan-Mamba	46.3112	0.9887	2.0229	2.6026	0.4338	0.5405	47.7171	0.9895	1.8430	2.1088	0.3610	0.3666	2109.30K
Sharpen	PNN	47.4524	0.9903	1.9168	2.3109	0.3789	0.4154	48.0758	0.9916	1.6883	2.0003	0.3462	0.3333	567.12K
	PanNet	47.0764	0.9884	1.9571	2.5526	0.3941	0.4446	48.2971	0.9906	1.6590	1.9593	0.3348	0.3115	799.76K
	INNformer	47.4650	0.9902	1.8877	2.3644	0.3766	0.4077	48.4220	0.9869	1.6935	1.9476	0.3304	0.3066	555.37K
	Pan-Mamba	46.7081	0.9858	2.1049	2.5384	0.4140	0.4941	47.8104	0.9874	1.7892	2.0647	0.3553	0.3451	970.55K
TR-MISR	PNN	47.1794	0.9905	1.9149	2.3223	0.3920	0.4450	47.7508	0.9908	1.7032	2.0278	0.3608	0.3671	692.43K
	PanNet	47.1593	0.9901	1.9001	2.3601	0.3944	0.4427	47.9199	0.9911	1.6909	1.9868	0.3549	0.3651	925.08K
	INNformer	47.1728	0.9863	1.8978	2.4066	0.3913	0.4347	48.2172	0.9895	1.7452	1.9890	0.3391	0.3297	680.69K
	Pan-Mamba	47.0933	0.9879	2.0055	2.4880	0.3943	0.4491	47.5771	0.9912	1.8942	2.1698	0.3679	0.3758	1095.87K

The bold entities represent the **best** results in each sub-block.

Table 2: Experimental metrics on WV3, GF2, and QB datasets

Methods	WV3				GF2				QB				
	PSNR↑	SSIM↑	SAM↓	ERGAS↓	PSNR↑	SSIM↑	SAM↓	ERGAS↓	PSNR↑	SSIM↑	SAM↓	ERGAS↓	
Sharpen	PNN [28]	35.9670	0.9504	4.6518	3.9014	40.5694	0.9641	1.9101	1.6791	35.7257	0.9222	5.5111	5.9618
	DicNN [14]	36.3114	0.9541	4.4815	3.7504	40.7252	0.9658	1.8568	1.6470	35.6112	0.9211	5.3824	6.0262
	MSDCNN [45]	35.3417	0.9399	5.1254	4.1817	40.5558	0.9643	1.9400	1.6862	35.5545	0.9201	5.4935	6.0724
	DRPNN [39]	36.5765	0.9562	4.4941	3.6001	41.3945	0.9693	1.7049	1.5391	36.7449	0.9367	5.1862	5.2610
	FusionNet [7]	36.4478	0.9567	4.4273	3.6040	41.0195	0.9673	1.7542	1.5953	36.2621	0.9311	5.4256	5.5555
SatFusion	Sharpen MISR	36.4483	0.9580	4.3532	3.6277	41.0877	0.9685	1.7861	1.5841	35.7310	0.9247	5.2484	5.9422
	PNN	36.0293	0.9518	4.8236	3.8285	41.6078	0.9692	1.6793	1.5126	35.9192	0.9256	5.2069	5.8500
	RAMS	37.0329	0.9608	4.1276	3.4447	41.7379	0.9693	1.6513	1.4934	36.2884	0.9291	5.1132	5.5815
	TR-MISR	36.7192	0.9591	4.3381	3.5696	41.7699	0.9695	1.6360	1.4894	36.0572	0.9275	5.1791	5.7769
	DicNN	37.6085	0.9654	3.8363	3.2232	42.3337	0.9731	1.4309	1.4096	36.8326	0.9397	5.0185	5.2307
MSDCNN	SRCCNN	37.8380	0.9660	3.7481	3.1560	42.6423	0.9740	1.3664	1.3712	37.7222	0.9480	4.5623	4.6345
	HighRes-Net	35.9792	0.9670	3.7040	3.1087	41.9437	0.9694	1.4461	1.4873	38.0532	0.9515	4.5044	4.4589
	RAMS	36.2144	0.9494	4.7771	3.8197	41.6595	0.9689	1.6937	1.5094	35.7382	0.9239	5.2642	5.9819
	TR-MISR	36.2069	0.9522	4.7088	3.7671	41.2276	0.9657	1.7653	1.5762	35.6936	0.9242	5.2186	5.9742
	DRPNN	36.8788	0.9595	4.2331	3.5196	42.4993	0.9738	1.4364	1.3783	37.4546	0.9452	4.8336	4.8230
FusionNet	SRCCNN	37.2064	0.9619	4.0026	3.3926	43.1166	0.9760	1.3685	1.2851	37.8682	0.9500	4.6161	4.5614
	HighRes-Net	37.2588	0.9618	4.0436	3.3597	43.5475	0.9775	1.3406	1.2095	37.9408	0.9500	4.5958	4.5190
	RAMS	38.3352	0.9698	3.5193	2.9545	43.4439	0.9774	1.2982	1.2333	38.0487	0.9526	4.4452	4.4753
	TR-MISR	38.1832	0.9682	3.5763	3.0154	43.8911	0.9793	1.2683	1.1717	37.8690	0.9514	4.4463	4.5625

The bold entities represent the **best** results in each sub-block.

6 Discussion

6.1 Practical Significance of SatFusion

Enhancing image quality. As an end-to-end unified framework, *SatFusion* unifies the advantages of existing fusion paradigms to

enhance reconstruction quality. Unlike MISR, which relies solely on multi-temporal data, it leverages high-resolution spatial details from the HRPAN image. Unlike conventional pansharpening that interpolates a single LRMS image, *SatFusion* achieves alignment by incorporating HR spatial features generated from complementary

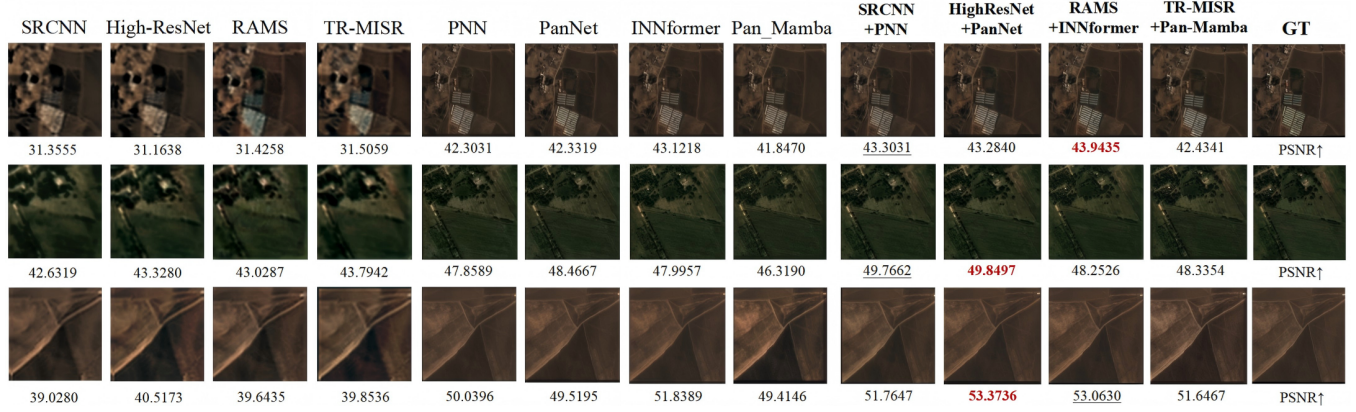


Figure 5: Quantitative comparison of PSNR for the fused images on the WorldStrat real-world dataset.

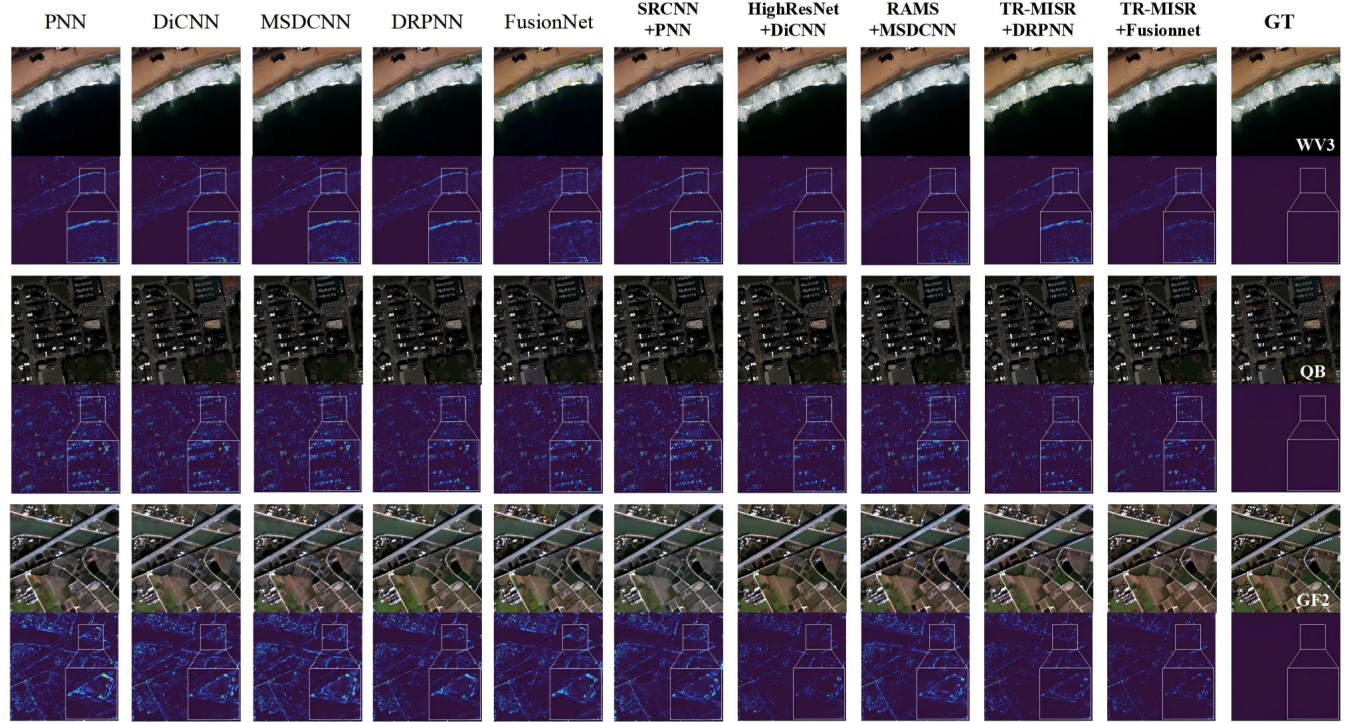


Figure 6: Qualitative comparison of error maps between the fused and ground-truth images.

multi-temporal observations. This design ensures robustness under motion blur and large modality gaps, effectively bridging the gap between redundant low-quality data and the demand for high-quality imagery in real-world Sat-IoT applications.

Reducing image redundancy. Traditional approaches typically store and transmit multiple images across temporal phases, leading to redundant transmission of overlapping information. In contrast, *SatFusion* consolidates multiple low-quality images into a single high-quality output, preserving information integrity while avoiding redundant storage and transmission. This naturally leads to a degree of data compression.

Assuming each pixel in every channel occupies one unit of storage space, let N denote the number of locations. Then the input data size is $D_{\text{input}} = N \times \left(T \cdot \frac{H}{Y} \cdot \frac{W}{Y} \cdot C_{ms} + H \cdot W \cdot 1 \right)$, and the output data size is $D_{\text{output}} = N \times (H \cdot W \cdot C_{ms})$. While redundancy reduction is guaranteed, the total physical data volume depends on specific conditions. Because the fused output typically has higher spatial resolution and more channels, the enhanced information richness may increase total data size. Only when T is sufficiently

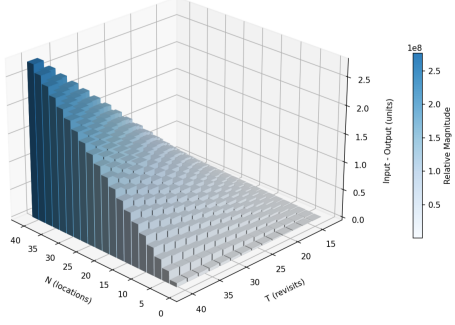


Figure 7: Difference in data volume between input and output images ($D_{\text{in}} - D_{\text{out}}, H(W) = 1024, \gamma = 4$)

large does the compression benefit outweigh this increase, satisfying $D_{\text{output}} < D_{\text{input}}$. As shown in Figure 7, this advantage becomes increasingly pronounced in Sat-IoT scenarios characterized by abundant multi-temporal data.

6.2 Future Prospects

SatFusion takes $\{l_{rms_t}\}_{t=1}^T$ and *Pan* as inputs, where the multi-temporal $\{l_{rms_t}\}_{t=1}^T$ images not only provide complementary information but also contribute to learning deep features aligned with *Pan*. However, in real-world scenarios, multi-temporal PAN images also exist but were not utilized in our design. Intuitively, incorporating multi-temporal PAN images through novel architectural designs could further improve fusion performance.

Moreover, *SatFusion* constitutes the first unified framework in the Sat-IoT domain that jointly optimizes high-quality image generation from both multi-temporal and multi-source data. Future research could extend this direction by exploring more sophisticated fusion architectures, adaptive loss balancing mechanisms, and lightweight model, further bridging the gap between theoretical fusion methods and real-world satellite applications.

7 Conclusion

In this paper, we propose ***SatFusion***, the first end-to-end unified framework that leverages multi-temporal and multi-source images for collaborative optimization to generate high-quality images, overcoming the limitations of task separation in existing methods. Quantitative and qualitative experiments conducted on the WorldStrat, WV3, GF2, and QB benchmark datasets demonstrate that *SatFusion* significantly improves fusion quality. Moreover, *SatFusion* maintains stable performance in challenging scenarios such as image blurring and large modality discrepancies. By alleviating the contradiction between redundant low-quality data and the demand for high-quality data, *SatFusion* better aligns with real-world Sat-IoT scenarios and holds strong potential for practical applications.

Acknowledgments

To Robert, for the bagels and explaining CMYK and color spaces.

References

- [1] Luciano Alparone, Lucien Wald, Jocelyn Chanussot, Claire Thomas, Paolo Gamba, and Lori Mann Bruce. 2007. Comparison of pansharpening algorithms: Outcome of the 2006 GRS-S data-fusion contest. *IEEE Transactions on Geoscience and Remote Sensing* 45, 10 (2007), 3012–3021.
- [2] Tai An, Xin Zhang, Chunlei Huo, Bin Xue, Lingfeng Wang, and Chunhong Pan. 2022. TR-MISR: Multiimage super-resolution based on feature fusion with transformers. *IEEE Journal of Selected Topics in Applied Earth Observations and Remote Sensing* 15 (2022), 1373–1388.
- [3] Wele Gedara Chaminda Bandara and Vishal M Patel. 2022. Hypertransformer: A textural and spectral feature fusion transformer for pansharpening. In *Proceedings of the IEEE/CVF conference on computer vision and pattern recognition*. 1767–1777.
- [4] Matteo Ciotola, Sergio Vitale, Antonio Mazza, Giovanni Poggi, and Giuseppe Scarpa. 2022. Pansharpening by convolutional neural networks in the full resolution framework. *IEEE Transactions on Geoscience and Remote Sensing* 60 (2022), 1–17.
- [5] Julien Cornebise, Ivan Oršolić, and Freddie Kalaitzis. 2022. Open high-resolution satellite imagery: The worldstrat dataset—with application to super-resolution. *Advances in Neural Information Processing Systems* 35 (2022), 25979–25991.
- [6] Bradley Denby and Brandon Lucia. 2020. Orbital edge computing: Nanosatellite constellations as a new class of computer system. In *Proceedings of the Twenty-Fifth International Conference on Architectural Support for Programming Languages and Operating Systems*. 939–954.
- [7] Liang-Jian Deng, Gemine Vivone, Cheng Jin, and Jocelyn Chanussot. 2020. Detail injection-based deep convolutional neural networks for pansharpening. *IEEE Transactions on Geoscience and Remote Sensing* 59, 8 (2020), 6995–7010.
- [8] Liang-Jian Deng, Gemine Vivone, Mercedes E Paoletti, Giuseppe Scarpa, Jiang He, Yongjun Zhang, Jocelyn Chanussot, and Antonio Plaza. 2022. Machine learning in pansharpening: A benchmark, from shallow to deep networks. *IEEE Geoscience and Remote Sensing Magazine* 10, 3 (2022), 279–315.
- [9] Michel Deudon, Alfredo Kalaitzis, Israel Goytom, Md Rifat Arefin, Zhichao Lin, Kris Sankaran, Vincent Michalski, Samira E Kahou, Julien Cornebise, and Yoshua Bengio. 2020. Highres-net: Recursive fusion for multi-frame super-resolution of satellite imagery. *arXiv preprint arXiv:2002.06460* (2020).
- [10] Chao Dong, Chen Change Loy, Kaiming He, and Xiaoou Tang. 2014. Learning a deep convolutional network for image super-resolution. In *Computer Vision–ECCV 2014: 13th European Conference, Zurich, Switzerland, September 6–12, 2014, Proceedings, Part IV 13*. Springer, 184–199.
- [11] Alexey Dosovitskiy, Lucas Beyer, Alexander Kolesnikov, Dirk Weissenborn, Xiaohua Zhai, Thomas Unterthiner, Mostafa Dehghani, Matthias Minderer, Georg Heigold, Sylvain Gelly, et al. 2020. An image is worth 16x16 words: Transformers for image recognition at scale. *arXiv preprint arXiv:2010.11929* (2020).
- [12] Yule Duan, Xiao Wu, Haoyu Deng, and Liang-Jian Deng. 2024. Content-adaptive non-local convolution for remote sensing pansharpening. In *Proceedings of the IEEE/CVF Conference on Computer Vision and Pattern Recognition*. 27738–27747.
- [13] Jing Gao, Peng Li, Zhikui Chen, and Jianing Zhang. 2020. A survey on deep learning for multimodal data fusion. *Neural Computation* 32, 5 (2020), 829–864.
- [14] Lin He, Yizhou Rao, Jun Li, Jocelyn Chanussot, Antonio Plaza, Jiawei Zhu, and Bo Li. 2019. Pansharpening via detail injection based convolutional neural networks. *IEEE Journal of Selected Topics in Applied Earth Observations and Remote Sensing* 12, 4 (2019), 1188–1204.
- [15] Xuanhua He, Ke Cao, Jie Zhang, Keyu Yan, Yingying Wang, Rui Li, Chengjun Xie, Danfeng Hong, and Man Zhou. 2025. Pan-mamba: Effective pan-sharpening with state space model. *Information Fusion* 115 (2025), 102779.
- [16] Sergio Herrera-Alonso, Miguel Rodríguez-Pérez, Raúl F Rodríguez-Rubio, and Fernando Pérez-Fontán. 2023. Improving uplink scalability of LoRa-based direct-to-satellite IoT networks. *IEEE Internet of Things Journal* 11, 7 (2023), 12526–12535.
- [17] Thorsten Hoeser, Felix Bachofer, and Claudia Kuenzer. 2020. Object detection and image segmentation with deep learning on Earth observation data: A review—Part II: Applications. *Remote Sensing* 12, 18 (2020), 3053.
- [18] Thorsten Hoeser and Claudia Kuenzer. 2020. Object detection and image segmentation with deep learning on earth observation data: A review—part i: Evolution and recent trends. *Remote Sensing* 12, 10 (2020), 1667.
- [19] Jacob Høxbroe Jeppesen, Rune Hylsberg Jacobsen, Fadiil Inceoglu, and Thomas Skjødeberg Toftgaard. 2019. A cloud detection algorithm for satellite imagery based on deep learning. *Remote sensing of environment* 229 (2019), 247–259.
- [20] Zi-Rong Jin, Tian-Jing Zhang, Tai-Xiang Jiang, Gemine Vivone, and Liang-Jian Deng. 2022. LAGConv: Local-context adaptive convolution kernels with global harmonic bias for pansharpening. In *Proceedings of the AAAI conference on artificial intelligence*, Vol. 36. 1113–1121.
- [21] Taeyeon Kim, Jeonghi Kwak, and Jihwan P Choi. 2021. Satellite edge computing architecture and network slice scheduling for IoT support. *IEEE Internet of Things journal* 9, 16 (2021), 14938–14951.
- [22] Vivek Kothari, Edgar Liberis, and Nicholas D Lane. 2020. The final frontier: Deep learning in space. In *Proceedings of the 21st international workshop on mobile computing systems and applications*. 45–49.
- [23] Israel Leyva-Mayorga, Marc Martínez-Gost, Marco Moretti, Ana Pérez-Neira, Miguel Ángel Vázquez, Petar Popovski, and Beatriz Soret. 2023. Satellite edge

computing for real-time and very-high resolution earth observation. *IEEE Transactions on Communications* 71, 10 (2023), 6180–6194.

[24] Jiaxin Li, Danfeng Hong, Lianru Gao, Jing Yao, Ke Zheng, Bing Zhang, and Jocelyn Chanussot. 2022. Deep learning in multimodal remote sensing data fusion: A comprehensive review. *International Journal of Applied Earth Observation and Geoinformation* 112 (2022), 102926.

[25] Qing Li and Daliang Xu. 2023. Satellite Computing: From Space to Your Screen. In *International Conference on Service-Oriented Computing*. Springer, 343–349.

[26] Ze Liu, Yutong Lin, Yue Cao, Han Hu, Yixuan Wei, Zheng Zhang, Stephen Lin, and Baining Guo. 2021. Swin transformer: Hierarchical vision transformer using shifted windows. In *Proceedings of the IEEE/CVF international conference on computer vision*. 10012–10022.

[27] Martina Lofqvist and José Cano. 2020. Accelerating deep learning applications in space. *arXiv preprint arXiv:2007.11089* (2020).

[28] Giuseppe Masi, Davide Cozzolino, Luisa Verdoliva, and Giuseppe Scarpa. 2016. Pansharpening by convolutional neural networks. *Remote Sensing* 8, 7 (2016), 594.

[29] Abbas Maskey and Mengu Cho. 2020. CubeSatNet: Ultralight Convolutional Neural Network designed for on-orbit binary image classification on a 1U CubeSat. *Engineering Applications of Artificial Intelligence* 96 (2020), 103952.

[30] Qinyang Meng, Wenxu Shi, Sijia Li, and Linlin Zhang. 2023. PanDiff: A novel pansharpening method based on denoising diffusion probabilistic model. *IEEE Transactions on Geoscience and Remote Sensing* 61 (2023), 1–17.

[31] Xiangchao Meng, Nan Wang, Feng Shao, and Shutao Li. 2022. Vision transformer for pansharpening. *IEEE Transactions on Geoscience and Remote Sensing* 60 (2022), 1–11.

[32] Muhammed T Razzak, Gonzalo Mateo-Garcia, Gurvan Lecuyer, Luis Gómez-Chova, Yarin Gal, and Freddie Kalaitzis. 2023. Multi-spectral multi-image super-resolution of Sentinel-2 with radiometric consistency losses and its effect on building delineation. *ISPRS Journal of Photogrammetry and Remote Sensing* 195 (2023), 1–13.

[33] Francesco Salvetti, Vittorio Mazzia, Aleem Khalid, and Marcello Chiaberge. 2020. Multi-image super resolution of remotely sensed images using residual attention deep neural networks. *Remote Sensing* 12, 14 (2020), 2207.

[34] Diego Valsesia and Enrico Magli. 2021. Permutation invariance and uncertainty in multitemporal image super-resolution. *IEEE Transactions on Geoscience and Remote Sensing* 60 (2021), 1–12.

[35] Ashish Vaswani, Noam Shazeer, Niki Parmar, Jakob Uszkoreit, Llion Jones, Aidan N Gomez, Łukasz Kaiser, and Illia Polosukhin. 2017. Attention is all you need. *Advances in neural information processing systems* 30 (2017).

[36] Lucien Wald, Thierry Ranchin, and Marc Mangolini. 1997. Fusion of satellite images of different spatial resolutions: Assessing the quality of resulting images. *Photogrammetric engineering and remote sensing* 63, 6 (1997), 691–699.

[37] Shangguang Wang and Qing Li. 2023. Satellite computing: Vision and challenges. *IEEE Internet of Things Journal* 10, 24 (2023), 22514–22529.

[38] Shangguang Wang, Qing Li, Mengwei Xu, Xiao Ma, Ao Zhou, and Qibo Sun. 2021. Tiansuan constellation: An open research platform. In *2021 IEEE International Conference on Edge Computing (EDGE)*. IEEE, 94–101.

[39] Yancong Wei, Qiangqiang Yuan, Huanfeng Shen, and Liangpei Zhang. 2017. Boosting the accuracy of multispectral image pansharpening by learning a deep residual network. *IEEE Geoscience and Remote Sensing Letters* 14, 10 (2017), 1795–1799.

[40] Piper Wolters, Favyen Bastani, and Aniruddha Kembhavi. 2023. Zooming out on zooming in: Advancing super-resolution for remote sensing. *arXiv preprint arXiv:2311.18082* (2023).

[41] Qiang Wu, Hongfei Zeng, Jin Zhang, Weishi Li, and Haojie Xia. 2024. A hybrid network of CNN and transformer for subpixel shifting-based multi-image super-resolution. *Optics and Lasers in Engineering* 182 (2024), 108458.

[42] Yinghui Xing, Litao Qu, Shizhou Zhang, Kai Zhang, Yanning Zhang, and Lorenzo Bruzzone. 2024. CrossDiff: Exploring self-supervised representation of pansharpening via cross-predictive diffusion model. *IEEE Transactions on Image Processing* 33 (2024), 5496–5509.

[43] Chen Yang, Qibo Sun, Qiyang Zhang, Hao Lu, Claudio A Ardagna, Shangguang Wang, and Mengwei Xu. 2024. Towards Efficient Satellite Computing Through Adaptive Compression. *IEEE Transactions on Services Computing* 17, 6 (2024), 4411–4422.

[44] Junfeng Yang, Xueyang Fu, Yuwen Hu, Yue Huang, Xinghao Ding, and John Paisley. 2017. PanNet: A deep network architecture for pan-sharpening. In *Proceedings of the IEEE international conference on computer vision*. 5449–5457.

[45] Qiangqiang Yuan, Yancong Wei, Xiangchao Meng, Huanfeng Shen, and Liangpei Zhang. 2018. A multiscale and multidepth convolutional neural network for remote sensing imagery pan-sharpening. *IEEE Journal of Selected Topics in Applied Earth Observations and Remote Sensing* 11, 3 (2018), 978–989.

[46] Roberta H Yuhas, Alexander FH Goetz, and Joe W Boardman. 1992. Discrimination among semi-arid landscape endmembers using the spectral angle mapper (SAM) algorithm. In *JPL Summaries of the Third Annual JPL Airborne Geoscience Workshop. Volume 1: AVIRIS Workshop*.

[47] Bing Zhang, Yuanfeng Wu, Boya Zhao, Jocelyn Chanussot, Danfeng Hong, Jing Yao, and Lianru Gao. 2022. Progress and challenges in intelligent remote sensing satellite systems. *IEEE Journal of Selected Topics in Applied Earth Observations and Remote Sensing* 15 (2022), 1814–1822.

[48] Yulun Zhang, Kunpeng Li, Kai Li, Lichen Wang, Bineng Zhong, and Yun Fu. 2018. Image super-resolution using very deep residual channel attention networks. In *Proceedings of the European conference on computer vision (ECCV)*. 286–301.

[49] Yuxuan Zheng, Jiaoqiao Li, Yunsong Li, Jie Guo, Xianyun Wu, and Jocelyn Chanussot. 2020. Hyperspectral pansharpening using deep prior and dual attention residual network. *IEEE transactions on geoscience and remote sensing* 58, 11 (2020), 8059–8076.

[50] Man Zhou, Jie Huang, Yanchi Fang, Xueyang Fu, and Aiping Liu. 2022. Pansharpening with customized transformer and invertible neural network. In *Proceedings of the AAAI conference on artificial intelligence*, Vol. 36. 3553–3561.

[51] Chunyu Zhu, Rongyuan Dai, Liwei Gong, Liangbo Gao, Na Ta, and Qiong Wu. 2023. An adaptive multi-perceptual implicit sampling for hyperspectral and multispectral remote sensing image fusion. *International Journal of Applied Earth Observation and Geoinformation* 125 (2023), 103560.

[52] Zhe Zhu and Curtis E Woodcock. 2012. Object-based cloud and cloud shadow detection in Landsat imagery. *Remote sensing of environment* 118 (2012), 83–94.

[53] Maciej Ziaja, Paweł Kowaleczko, Tomasz Tarasiewicz, Daniel Kostrzewa, and Michał Kawulok. 2025. Hyperspectral Pansharpening Enhanced With Multi-Image Super-Resolution for PRISMA Data. *IEEE Journal of Selected Topics in Applied Earth Observations and Remote Sensing* (2025).

A Hyperparameter Experiments

We address **RQ3** by varying two key hyperparameters.

We first change the number of input multi-temporal images T on the original WorldStrat dataset. As shown in Figure 8, the quality of image fusion improves as the number of multi-temporal images increases. In particular, the evaluation metrics show significant improvement when the number of images increases in the early stage, indicating that incorporating more multi-temporal data is beneficial for the model performance. However, when the number of images continues to increase, the metrics tend to stabilize. We attribute this to two reasons: (1) limitations of the model architecture design, and (2) the fact that introducing more multi-temporal data brings not only complementary information but also more noise [2], which constrains further performance gains.

We also vary the super-resolution scaling factor γ on the original WorldStrat dataset. As shown in Table 3, *SatFusion* achieves the best performance at scaling factors $\gamma = 2, 5$ (In Table 1, $\gamma \approx 3$). Moreover, for relatively small scaling factors, the fused super-resolved MS images SR produced by *SatFusion* exhibit more stable quality.

B Ablation Studies

We address **RQ4** by conducting ablation experiments on both the loss function components and the Fusion Composition module.

We design different weighted combinations of loss functions to supervise the reconstruction results, jointly optimizing both texture

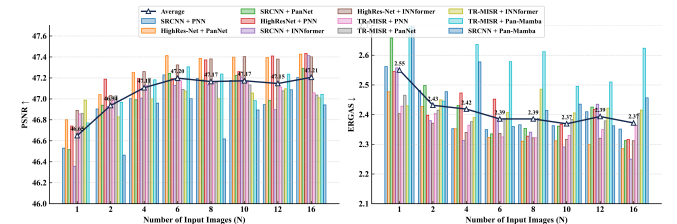


Figure 8: Changes in metrics for different fusion methods as the number of input multi-temporal images T increases.

Table 3: Quantitative results at scales $\uparrow \times 2$ and $\uparrow \times 5$.

Method ($\uparrow \times 2$)		PSNR \uparrow	SSIM \uparrow	SAM \downarrow	ERGAS \downarrow
MISR	HighRes-Net	37.9059	0.8886	2.0946	8.3164
	RAMS	38.1640	0.8925	2.0828	7.9090
Sharpen	PNN	47.2997	0.9878	2.0600	2.4596
	Pan-Mamba	45.7863	0.9861	2.9941	2.9944
SatFusion	HighRes-Net+PNN	48.1212	0.9904	1.8379	2.1995
	RAMS+Pan-Mamba	47.5778	0.9878	1.9370	2.4856
Method ($\uparrow \times 5$)		PSNR \uparrow	SSIM \uparrow	SAM \downarrow	ERGAS \downarrow
MISR	SRCNN	35.5189	0.8543	2.5564	8.5944
	TR-MISR	35.6686	0.8568	2.6219	8.3854
Sharpen	PanNet	44.7126	0.9806	2.4406	3.0794
	INNformer	45.5145	0.9843	2.4934	2.7632
SatFusion	SRCNN+PanNet	46.1587	0.9888	2.1801	2.5405
	TR-MISR+INNformer	46.3109	0.9887	2.0627	2.4422

The bold entities represent the **best** results.

and spectral features of the images. We perform ablation studies on the loss components using the original WorldStrat dataset. As shown in Table 4, the worst metrics are highlighted in bold. Removing any single loss term leads to a significant degradation in certain evaluation metrics, confirming that our multi-loss optimization effectively balances performance and perceptual quality.

Table 4: Quantitative results with different loss functions.

Method	\mathcal{L}_{MAE}	\mathcal{L}_{MSE}	$\mathcal{L}_{\text{SSIM}}$	\mathcal{L}_{SAM}	PSNR \uparrow	SSIM \uparrow	SAM \downarrow	ERGAS \downarrow
SRCNN	✓	✓	✓	✓	47.2319	0.9898	2.0082	2.3719
	✓	✓	✓	✗	47.1817	0.9896	2.1779	2.4117
	✓	✓	✗	✓	46.8231	0.9904	1.9193	2.5160
	✓	✗	✗	✗	47.3082	0.9908	2.0869	2.3874
HighRes-Net	✓	✓	✓	✓	47.3911	0.9902	1.9508	2.3232
	✓	✓	✓	✗	47.5657	0.9903	1.9903	2.2592
	✓	✓	✗	✓	46.7710	0.9889	1.8810	2.5688
	✓	✗	✗	✗	47.4274	0.9875	1.9866	2.2876
RAMS	✓	✓	✓	✓	47.4650	0.9902	1.8877	2.3635
	✓	✓	✓	✗	47.5535	0.9871	2.0989	2.3782
	✓	✓	✗	✓	47.0930	0.9869	1.8974	2.4393
	✓	✗	✗	✗	47.6293	0.9862	2.3441	2.5325
+INNformer	✓	✓	✓	✓	47.0933	0.9879	2.0055	2.4880
	✓	✓	✓	✗	47.3086	0.9860	2.2099	2.5095
	✓	✓	✗	✓	46.4710	0.9832	2.0040	2.7849
	✓	✗	✗	✗	47.2311	0.9854	2.4206	2.7564

The bold entities represent the **worst** results.

The Fusion module consists of residual connections and convolutional adjustment operations. Compared with synthetic datasets, the real datasets exhibit more noticeable spectral differences between the multi-temporal images and the HRMS images. We conduct ablation on the convolutional adjustment operation using the original WorldStrat dataset. As shown in Table 5, removing the convolutional adjustment operation results in a drop in most metrics and visible color distortions, thereby reducing perceptual quality. We also observe that for a few methods (e.g., Pan-Mamba), the convolutional adjustment operation has limited influence. However, as a general framework that should adapt to a wide range of prior works, including the convolutional adjustment operation is necessary.

Table 5: Ablation study on the effect of convolutional adjustment operation.

Method	Adjust	PSNR \uparrow	SSIM \uparrow	SAM \downarrow	ERGAS \downarrow
HighRes-Net+PNN	✓	47.3835	0.9914	1.9368	2.3304
	✗	47.1994	0.9891	1.9714	2.3433
HighRes-Net+INNformer	✓	47.4021	0.9902	1.8958	2.3094
	✗	47.3280	0.9897	1.9413	2.3210
TR-MISR+INNformer	✓	47.1728	0.9863	1.8978	2.4066
	✗	46.7988	0.9851	2.0015	2.5120
RAMS+INNformer	✓	47.4650	0.9902	1.8877	2.3635
	✗	47.1385	0.9876	1.9411	2.4032
TR-MISR+PanNet	✓	47.1593	0.9901	1.9001	2.3601
	✗	47.1296	0.9898	1.8937	2.3658
HighRes-Net+Pan-Mamba	✓	46.3112	0.9887	2.0229	2.6026
	✗	46.3500	0.9909	2.2393	2.6687
TR-MISR+Pan-Mamba	✓	47.0933	0.9879	2.0055	2.4880
	✗	47.0768	0.9899	2.0514	2.4806

The bold entities represent the **better** results.

C Robustness Experiments

We address **RQ5** by varying the noise level to evaluate model robustness.

To further validate the robustness and generalization ability of the proposed method in complex remote sensing scenarios, we conducted experiments on a synthetic dataset by introducing a control parameter ϵ to jointly adjust the intensity of noise perturbations, thereby simulating the instabilities commonly observed in real multi-temporal remote sensing imagery.

Specifically, the pixel displacement range was randomly set within 2 pixels, the noise intensity was defined as 0.1ϵ , and the brightness shift range was $[1 - 0.05\epsilon, 1 + 0.05\epsilon]$. At each ϵ level, we compared the performance of *SatFusion* with that of pansharpening networks, in order to evaluate the model's adaptability to perturbations as well as the contribution of multi-temporal information to robustness improvement.

As shown in Figure 9, the experimental results indicate that as ϵ increases, the degradation of fused image quality in *SatFusion* is more gradual, suggesting that the method can maintain stable performance even under challenging conditions such as severe image blurring and significant cross-modal discrepancies.

D Details of Loss Computation

As emphasized in the main text, we ensured consistency in loss computation throughout the experiments so that the optimization of evaluation metrics directly demonstrates the effectiveness of the proposed architecture. This section provides a detailed description of the loss computation process.

We conducted experiments on the WorldStrat, WV3, QB, and GF2 datasets. Previous works commonly use the WV3, QB, and GF2 datasets to construct artificial datasets via the Wald protocol for training Pansharpening networks. In our experiments validating that integrating Pansharpening networks into *SatFusion* can improve fusion quality and robustness, we modified the DLPan-Toolbox codebase [8]. This codebase, which evaluates the effectiveness of Pansharpening network structures using WV3, QB, and GF2, integrates networks such as FusionNet and DRPNN. Based

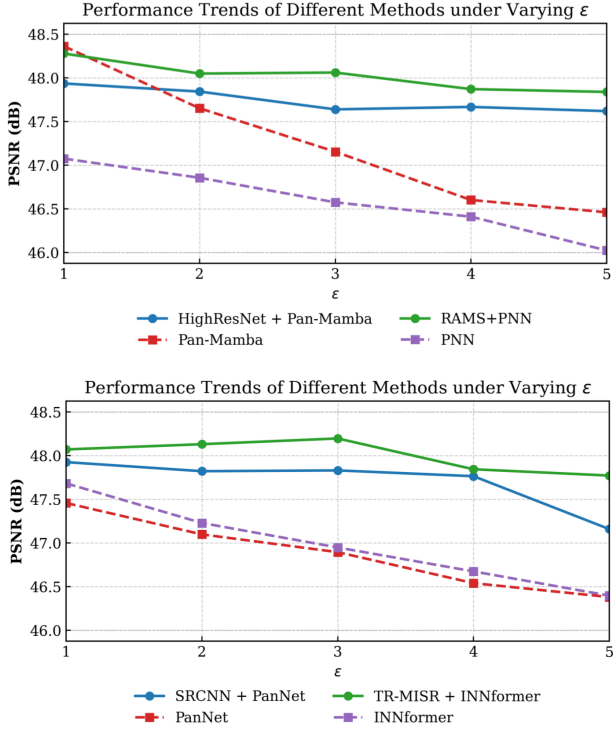


Figure 9: PSNR comparison under different perturbation levels ϵ . *SatFusion* incorporating multi-temporal information consistently show higher reconstruction quality, demonstrating stronger robustness.

on this codebase, we built the *SatFusion* framework by integrating MISR networks with Pansharpening networks, while also adjusting the input data (as shown in Fig. 6(b)). In these experiments, *SatFusion* and Pansharpening networks adopted exactly the same experimental configurations (training epochs, batch size, optimizer, etc.) and the same loss functions as the original Pansharpening network training, to demonstrate the generalizability of *SatFusion*'s ability to enhance prior work.

Previous studies often employ the WorldStrat real dataset for MISR network training. In experiments on this dataset validating the integration of Pansharpening networks into *SatFusion*, we followed prior work by performing image adjustment before loss computation to address global brightness bias [2, 9, 33]. Specifically, we corrected the overall brightness of the *SatFusion* output HRMS image to match that of the ground truth HRMS image by computing the mean bias channel-wise:

$$\mu_{GT} = \frac{1}{H \times W} \sum_{i=1}^H \sum_{j=1}^W GT_{i,j}, \quad \mu_{SR} = \frac{1}{H \times W} \sum_{i=1}^H \sum_{j=1}^W SR_{i,j},$$

$$SR = SR + \mu_{GT} - \mu_{SR}.$$

Here, μ_{GT} denotes the overall brightness of the ground truth HRMS image, while μ_{SR} denotes the overall brightness of the *SatFusion* output HRMS image. The brightness compensation is applied channel-wise.

To handle potential image misalignment, *SatFusion* crops both GT and SR to compensate for spatial shifts and returns the minimum loss value [5]. Cropping is implemented using a Lanczos convolution kernel. Lanczos is a high-quality image resampling filter based on the sinc function. It achieves a balance between computational efficiency and anti-aliasing by truncating the infinite support of the sinc function with a window function, thereby reducing ringing artifacts while preserving sharpness. The initial offset x is generated from p_x (absolute shift), $step$ (shift stride), and a (kernel lobes):

$$r = start, start + 1, \dots, end,$$

$$d = -px, -px + step, -px + 2step, \dots, px,$$

$$x_i = r_1 - d_i, r_2 - d_i, \dots, r_{width} - d_i,$$

where $start = -a - px$, $end = a + px$, and $width$ is the length of r . A sinc filter is then applied to generate a 1D kernel L , which is extended to a 2D Lanczos kernel for image shifting. For each shifted ground truth image GT'_i , we align it with the cropped SR' and compute the loss, selecting the minimum as the final result:

$$L_i = a \cdot \text{sinc}(\pi \cdot x_i) \cdot \text{sinc}\left(\frac{\pi \cdot x_i}{a}\right), \quad \text{Lanczos} = L \otimes L,$$

$$GT'_i = \text{Lanczos}_i(GT), \quad SR' = \text{patch}(SR),$$

$$\text{loss} = \min \text{Loss}(GT'_i, SR').$$

Here, $\text{patch}(\cdot)$ is a cropping function that adjusts the image size to match GT'_i . Loss refers to the composite weighted loss introduced in Section 4.3, with weights $\lambda_1 = 0.3$, $\lambda_2 = 0.3$, $\lambda_3 = 0.2$, and $\lambda_4 = 0.2$.

E Details of Experimental Parameter Settings

As emphasized in the main text, we ensured the consistency of experimental configurations, i.e., *SatFusion* and baseline methods were compared under the same training and data parameter settings. This section provides the detailed parameter configurations used in the experiments.

The WorldStrat dataset provides MISR network codes as baselines, including SRCNN and HighRes-Net. In addition, we incorporated other representative MISR methods (RAMS, TR-MISR) and representative Pansharpening methods (PNN, PanNet, INNformer, Pan-Mamba). For experiments conducted on this dataset, the original parameters in the source codebase were preserved [5]. Specifically, the training parameters were set as: batch size = 16, optimizer = Adam, and maximum epochs = 20. The data parameters included consistent train/validation/test splits, with $H = W = 156$, $\frac{H}{y} = \frac{W}{y} = 50$ ($y \approx 3$), $C_{ms} = 3$, $T = 8$, $C_{\text{hidden_encode}} = 128$, $C_{\text{MISR}} = 128$. Here, to ensure that C_{MISR} is divisible by y^2 , the parameter y of the PixelShuffle Block is set to 2. In all other cases, the PixelShuffle Block parameter y is identical to the image spatial upscaling factor y .

Extensive studies of Pansharpening networks have been conducted on the WV3, QB, and GF2 datasets. The DLPan-Toolbox codebase provides corresponding implementations of Pansharpening methods. We used five representative baselines: PNN, DiCNN, MSDCNN, DRPN, and FusionNet, and incorporated MISR networks into *SatFusion*. In experiments on these datasets, the data parameters were consistent with the source codebase, while training parameters were set individually for different Pansharpening methods [8]. Taking WV3 as an example, the experimental configurations (with reduced epochs compared to the original codebase

for efficiency, in fact the model has already converged) were as follows. For training and validation: $H = W = 64$, $\frac{H}{\gamma} = \frac{W}{\gamma} = 16$ ($\gamma = 4$), $C_{ms} = 8$, $T = 8$, $C_{hidden_encode} = 128$, $C_{MISR} = 128$. For testing: $H = W = 256$, $\frac{H}{\gamma} = \frac{W}{\gamma} = 64$ ($\gamma = 4$), with other parameters consistent with those of the training and validation sets.

Table 6: Training parameters for different methods.

Parameters	PNN	DiCNN	MSDCNN	DRPNN	FusionNet
Epochs	1000	1000	500	500	400
Batch Size	64	64	64	32	32
Optimizer	SGD	Adam	Adam	Adam	Adam
Loss Function	l_2	l_2	l_2	l_2	l_2

All experimental code has been open-sourced. Experiments were conducted on a server equipped with eight NVIDIA RTX 4090 GPUs to ensure reproducibility.